Supplementary Information (SI) for Nanoscale.

Supplementary Information for

Nanophotonics of mid-infrared plasmon-polaritons in interfaces between metals and two-dimensional crystals

Flávio H. Feres[a]*, Ingrid D. Barcelos[a], Dario A. Bahamon[b,c], João E. Levandoski[d], Andrea Mancini[e], Thiago M. dos Santos[a], Rafael A. Mayer[a,f], Davi H. S. Camargo[g], Carlos C. B. Bufon[h], Adrian Cernescu[i], Stefan A. Maier[j,k] , Raul de O. Freitas[a] and Francisco C. B. Maia[a]*

[a.] *Brazilian Synchrotron Light Laboratory (LNLS), Brazilian Center for Research in Energy and Materials (CNPEM), Zip Code 13083-970, Campinas, Sao Paulo, Brazil.*

[b.] *MackGraphe –Graphene and Nanomaterials Research Institute, Mackenzie Presbyterian University, São Paulo -01302-907, Brazil.*

[c.] *School of Engineering, Mackenzie Presbyterian University, São Paulo - 01302-907, Brazil*

[d.] *Department of Materials and Bioprocesses Engineering, School of Chemical Engineering, University of Campinas, Campinas, Brazil*

[e.] *Chair in Hybrid Nanosystems, Nanoinstitute Munich, Ludwig-Maximilians-Universität Munich, Königinstrasse 10, 80539 Munich, Germany*

[f.] *Physics Department, Gleb Wataghin Physics Institute, University of Campinas (Unicamp), 13083-859 Campinas, Sao Paulo, Brazil*

[g.] *Brazilian Laboratory of Nanotechnology (LNNano), Brazilian Center for Research in Energy and Materials (CNPEM), Zip Code 13083-970, Campinas, Sao Paulo, Brazil.*

[h.] *Institute of Geosciences and Exact Sciences, São Paulo State University (UNESP), Rio Claro, Brazil*

[i.] *Attocube systems AG, 85540, Haar-Munich, Germany.*

[j.] *School of Physics and Astronomy, Monash University, Clayton, 3800, VIC, Australia*

[k.] *Blackett Laboratory, Imperial College London, London, SW7 2AZ, UK.*

*Corresponding authors: francisco.maia@lnls.br, flavio.feres@lnls.br

Summary

I. The damped plane wave model

Fig. S1 presents the illumination scheme of the s-SNOM tip probing the hBN/Au/SiO_2 heterostructure near the edge of the Au film. In this case, the excitation induces strong light confinement at the tip apex and the Au edge due to antenna effect. Hence, tip at $\mathbf{x}$ and edge at $\mathbf{x} = \mathbf{0}$ are turned into the optical near-field sources launching polariton waves. It is worthy to remark that only waves reaching the tip are probed, i.e scattered by the tip to the detector. The edge-launched waves (E_{SPP}^{e} and E_{HPhP}^{e}) travelling in the $\hat{\mathrm{x}}$ direction reach the tip. But the tip-launched waves (E_{SPP}^{t} and E_{HPhP}^{t}), propagating in $-\hat{\mathrm{x}}$, do not return to the tip since they are not back-reflected by any reflecting feature in our system. Such fact is confirmed by experimental observations showing no evidence of waves with spatial periods of half wavelengths, which would characterize a reflected wave. Therefore, the modelling considers that the near-field light scattered by the tip is a result from the interference among edge-launched polaritons and a non-propagative term (background). It is assumed that these waves are described by damped plane waves as the edge can be seen as a linear launcher composed of multiple sources. Taking into account the SPPs on Au and the HPhPs in the hBN, the resulting optical field is given by

$$\mathrm{E} = \mathrm{A_{HPhP}} \mathrm{e}^{-\mathrm{i}(\mathrm{q_{HPhP}} - \mathrm{i}\gamma_{\mathrm{HPhP}})\mathrm{x} - \mathrm{i}\delta} + \mathrm{A_{SPP}} \mathrm{e}^{-\mathrm{i}.(\mathrm{q}_{SPP} - \mathrm{i}\gamma_{\mathrm{SPP}})\mathrm{x}} + \mathrm{C} \qquad \text{(Eq. S1),}$$

where the waves are defined by amplitude A_{α}, momentum q_{α} and damping γ_{α}, with $\alpha = \mathrm{SPP}$ or HPhP. C is complex non-propagative background and δ, the relative phase difference between the waves. Eq. S1, the same as Eq. 1, is used in the fits.

In addition, we account for the interference between the SPP wavevector (q_{SPP}) and the illumination (k_0) following Figure S1. In our system, all measurements were performed under perpendicular illumination ($\varphi = 0$, in Fig S1). Thus, the effective wavevector (k_{ef}) is given as follows: $\mathrm{k}_{ef} = \mathrm{q}_{SPP} - \mathrm{k}_0 \sin\theta$. Moreover, the measured fringe period (λ_{ef}) is given by $\lambda_{ef} = \frac{\lambda_{SPP}}{1-(\lambda_{SPP}/\lambda_0)\sin\theta}$. This consideration is in concordance with the references[1–5]

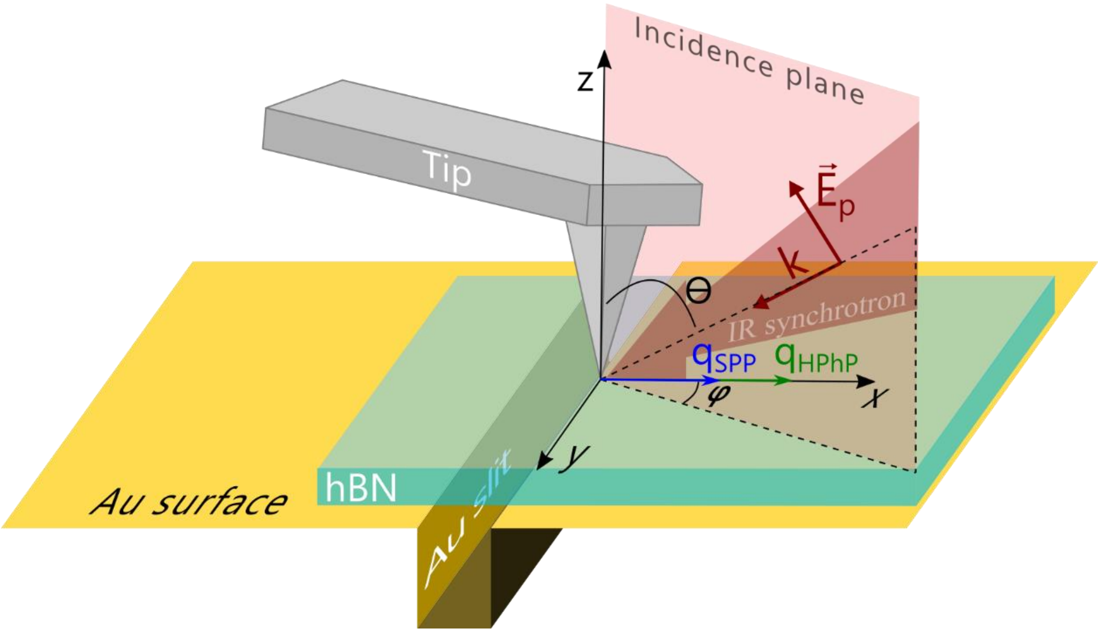

***Figure S1** – Reference frame for the model-fit.*

II. Fourier Transform of profiles of hBN/Au/SiO_2 and Au/SiO_2 images illuminated at ω = 1470 cm^{-1}.

Figure S2 shows the images of hBN/Au/SiO_2 (Fig S1a) and Au/SiO_2 (Fig. S1d) and corresponding profiles and their model-fits (Fig. S2b and S2e). Those figures are the same as shown in Fig. 1d-g of the main manuscript. In Fig. S2c and S2f, the Fourier Transforms of the profiles in S2b and S2e are displayed. It is observed that peaks corresponding to the SPP and HPhP rise only for P_1' and P_2', thus, validating our choices in the fitting analyses.

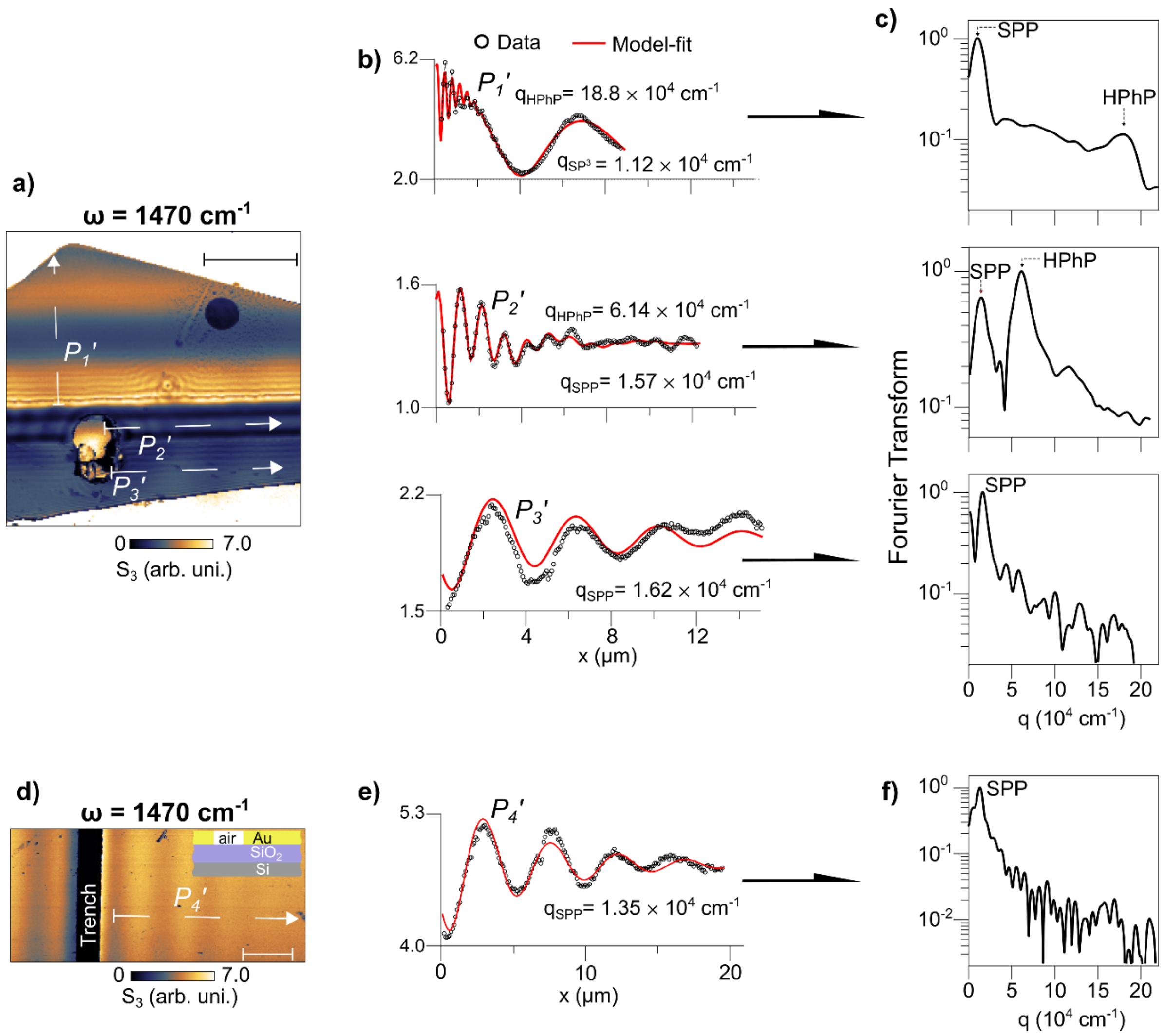

Figure S2 *- Same as in Fig. 1 of the main text:* ***a****) S_3 image of hBN/Au/SiO_2 illuminated at $\omega = 1470\ cm^{-1}$ and* ***b****) extracted profiles from (****a****) and corresponding model-fits.* ***c****) Fourier Transform of the profiles in (****b****).* ***d****) S_3 image Au/SiO_2 illuminated at $\omega = 1470\ cm^{-1}$.* ***e****) profile P_4' and the corresponding fit.* ***f****) Fourier Transform of P_4'.*

III. Experimental Dispersion by One-Sided Fourier Transform

The frequency dispersion relation $\omega - \boldsymbol{q_{SSP}}$ plots of the main manuscript are constructed from eq. S2

$$Re[\mathfrak{F}(q,\omega)] = \frac{1}{\sqrt{2\pi}}\left[\frac{q_{SPP}(\omega)}{(q_{SPP} - q)^2 + \gamma_{SPP}^2(\omega)}\right] \tag{S2}$$

that is the real part of the normalized damped plane wave (eq. S1)

$$\mathrm{E}(x) = \begin{cases} 0 & -\infty < x < 0 \\ e^{-i.(q_{SPP} - i\gamma_{SPP})x} & 0 \le x < \infty \end{cases} \quad \text{(S3)},$$

which is defined for positives values of position ($0 \le x < \infty$).

We also present in Figure S3 the $\mathrm{Re}[\mathfrak{F}(q,\omega)]$ for different ω's is resonant with the corresponding momentum. It is seen that the damping value modulates the full width at a half maximum of $\mathrm{Re}[\mathfrak{F}(q,\omega)]$.

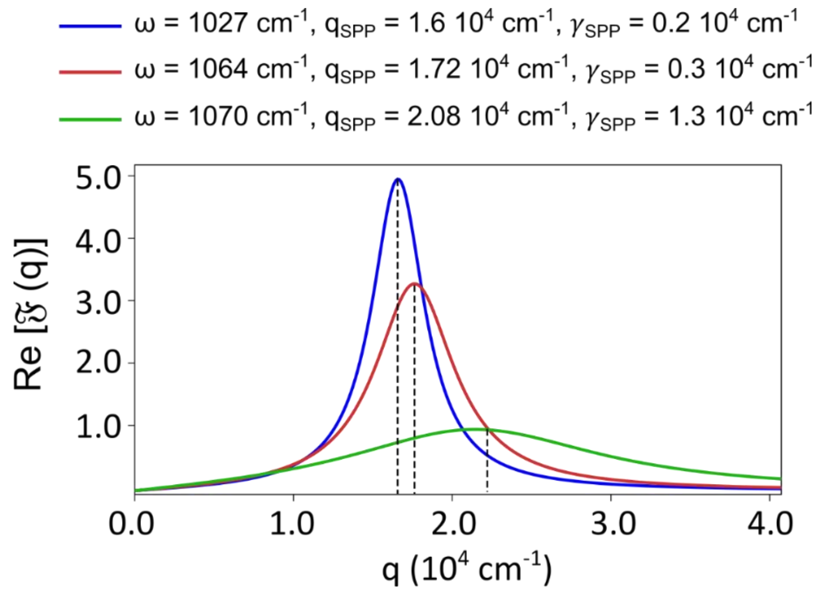

Figure S3 – *Behavior of* $\mathrm{Re}[\mathfrak{F}(q,\omega)]$ *for different values of momentum and damping.*

IV. Hyperbolic Phonon Polaritons Dispersion Relation

The dispersion relation of hyperbolic phonon polaritons (HPhPs) was extracted using the same methodology outlined in the previous section. Figure S4a presents the amplitude of the second harmonic (S_2) derived from the spectral linescan performed on the hBN/Au sample. The observed small fringes in the figure correspond to the propagation of HPhP modes, reflecting the characteristic interference patterns generated by these polaritonic waves.

In Figure S4b, the experimental HPhP dispersion relation, obtained through FT analysis, is displayed. Overlaid on this plot is a white dashed line representing the theoretical prediction for a three-layer system: Air/hBN(70 nm)/Au. This theoretical model accounts for the layered structure of the sample, incorporating the 70 nm thick hexagonal boron nitride (hBN) layer atop a gold (Au) substrate, with air as the surrounding medium. The comparison between experimental data and the theoretical curve provides critical insights into the behavior of HPhPs in this heterostructure, validating the model and offering a deeper understanding of the polaritonic properties in such systems.

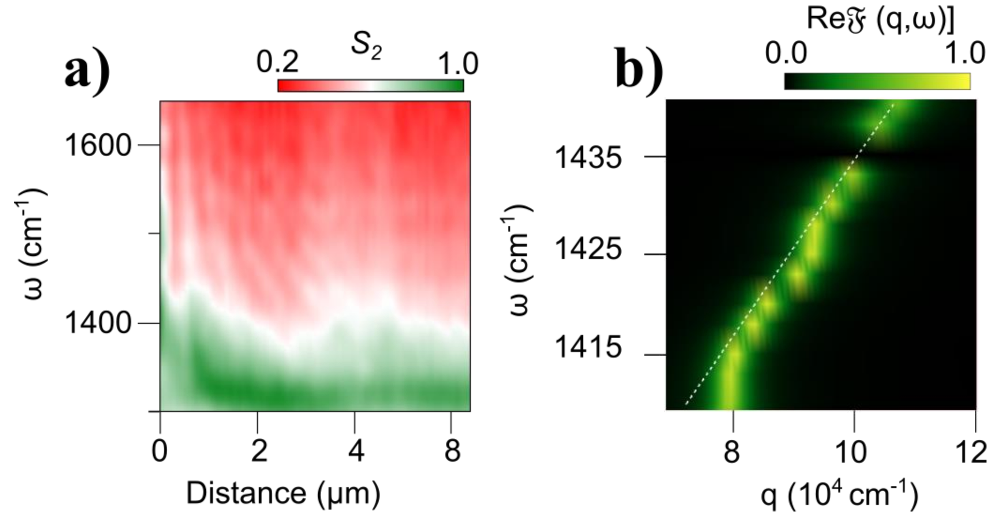

Figure S4 *– a) Amplitude of the second harmonic (S_2) of a spectral linescan performed in a 70 nm thick hBN crystal. B) HPhP dispersion relation obtained via* $\mathrm{Re}[\mathfrak{F}(q,\omega)]$. *The white dashed line represents the theoretical prediction.*

V. Surface Plasmons Polaritons in Air/Au/SiO_2

In Fig. S5a, it is presented a SINS spectral linescan on Au (90 nm thick) / SiO_2 (2 μm) unveiling the existence of SPP waves (black arrows). In Fig. S4b we show the theoretical $\omega - \boldsymbol{q_{SSP}}$ calculated from the multilayer model[6] for air/Au/SiO_2. The $\omega - \mathrm{q_{SSP}}$ experimental data (green circles), determined from the model fit as explained in the main manuscript, are also plotted in Fig. S5b. It is noted good agreement between theory and experiment further confirming the generality of the mid-IR SPP waves and our modelling. To compare, we the theoretical dispersion for the Au/SiO_2 interface (white dashed line in Fig. S5b) considering these materials filling the semi-infinity super and substrate (white dashed line shown in Fig S5b).

We note that the AC region near the SiO_2 optical phonons manifest itself both in the theoretical and in the experimental dispersions. The group velocity ($\mathrm{v_g} = \frac{\partial\omega}{\partial q}$) and lifetime ($\tau = \frac{L_x}{\mathrm{v_g}}$) for the modes can be achieved theoretically

(Figure S5c and S4d). We see that v_g and τ in Au/SiO$_2$ differ from those in hBN/Au/SiO$_2$ indicating by changing the IMI heterostructure one can also modulate such photonic parameters.

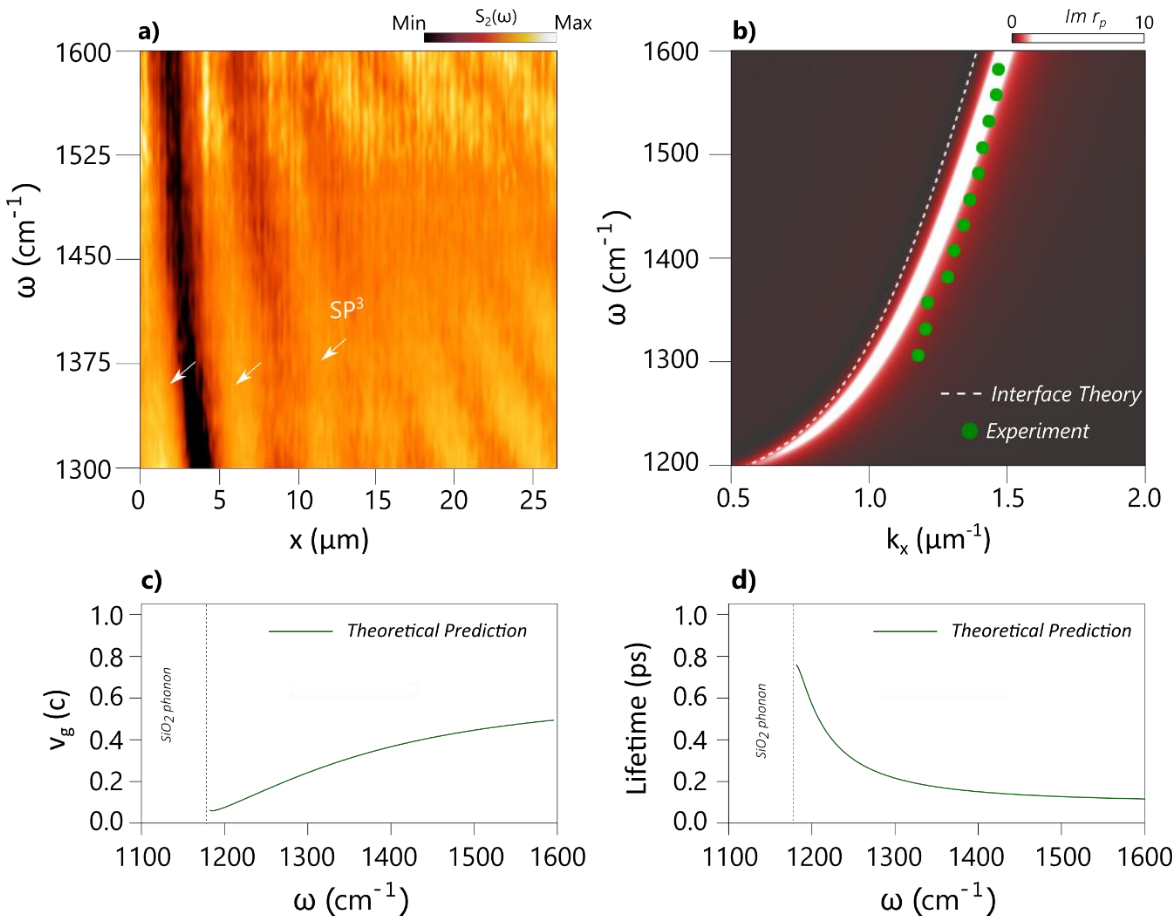

Figure S5- *a) SINS spectral linescan on Au(90 nm)/SiO$_2$. b) Theroerical $\omega - q_{SSP}$ (map) from eq. S16 and experimental $\omega - q_{SSP}$ (green circles) extracted from the fittings profiles extracted from a). c) and d) theoretical prediciton of v_g and τ for the polaritons modes*

VI. Coupled Harmonic Oscillators Model

The coupling regime between the SPP waves and the phonons is assessed by the two coupled harmonic oscillators[7–9] model that is characterized by the coupled equations of motion (S4)

$$\begin{cases} \ddot{x}_{SPP}(t) + \Gamma_{SPP}\dot{x}_{SP}(t) + \omega_{SPP}^2 x_{SPP}(t) - \Omega\overline{\omega}x_{PP}(t) = F_{SPP}(t) \\ \ddot{x}_{PP}(t) + \Gamma_{PP}\dot{x}_{PP}(t) + \omega_{PP}^2 x_{PP}(t) - \Omega\overline{\omega}x_{SPP}(t) = F_{PP}(t) \end{cases} \quad \text{(S4)},$$

where ω_{SSP}, Γ_{SSP} and x_{SPP} are the frequency, damping and displacement of the SPP modes respectively. The corresponding parameters of the phonons modes are indexed with PP. Ω represents the coupling strength. By definition, $\overline{\omega} = (\omega_{SP} + \omega_{PP})/2$. F_{PP} and F_{SP} are the effective forces that give energy to the system and are proportional to the external electric field. Considering harmonic time-dependent solutions, $Ae^{-i\omega t}$, equation (S4) can be written as (S5)

$$\begin{cases}(-\omega^2 - i\Gamma_{SPP}\omega + \omega_{SPP}^2)x_{SP} - \Omega\bar{\omega}x_{PP} = F_{SPP} \\ (-\omega^2 - i\Gamma_{PP}\omega + \omega_{PP}^2)x_{PP} - \Omega\bar{\omega}x_{SPP} = F_{PP}\end{cases} \quad \text{(S5).}$$

Denoting $\Delta_1 = -\omega^2 - i\Gamma_{SP}\omega + \omega_{SP}^2$, $\Delta_2 = \Omega\bar{\omega}$ and $\Delta_3 = -\omega^2 - i\Gamma_{PP}\omega + \omega_{PP}^2$, we can rewrite (S5) as following

$$\mathbf{A}\begin{pmatrix} x_{SP} \\ x_{PP} \end{pmatrix} = \begin{pmatrix} F_{SP} \\ F_{PP} \end{pmatrix}; \;\; \mathbf{A} = \begin{pmatrix} \Delta_1 & -\Delta_2 \\ -\Delta_2 & \Delta_3 \end{pmatrix} \quad \text{(S6)}$$

$$\begin{pmatrix} x_{SP} \\ x_{PP} \end{pmatrix} = \mathbf{A}^{-1}\begin{pmatrix} F_{SP} \\ F_{PP} \end{pmatrix} \quad \text{(S7)}$$

From (S7), ω_{SP} and ω_{PP} can be easily calculated

$$x_{SP}(t) = \left(\frac{\Delta_3 F_{SP} + \Delta_2 F_{PP}}{\text{Det}\,\mathbf{A}}\right)e^{-i\omega t} \quad \text{(S8)}$$

$$x_{PP}(t) = \left(\frac{\Delta_2 F_{SP} + \Delta_1 F_{PP}}{\text{Det}\,\mathbf{A}}\right)e^{-i\omega t} \quad \text{(S9)}$$

Thus, with the solutions for the equation of motion, we can calculate the extinction coefficient $C_{\text{ext}}(\omega)$, eq. S10, which is proportional to the power loss of the coupling mechanism.

$$C_{\text{ext}}(\omega) \propto \langle F_{PP} \cdot \dot{x}_{PP} + F_{SP} \cdot \dot{x}_{SP} \rangle \quad \text{(S10)}$$

$$C_{\text{ext}}(\omega) \propto \text{Im}\left[\frac{\Delta_3}{\text{Det}\,\mathbf{A}}\right]{F_{SP}}^2\omega + \text{Im}\left[\frac{\Delta_1}{\text{Det}\,\mathbf{A}}\right]{F_{PP}}^2\omega + 2\text{Im}\left[\frac{\Delta_2}{\text{Det}\,\mathbf{A}}\right]F_{PP}F_{SP}\omega \quad \text{(S11)}$$

Following the same method of ref. [7], $C_{\text{ext}}(\omega)$ is assumed to be proportional to the $\mathfrak{F}(q,\omega)$ in the iso-momentum regime. Furthermore, using the approximation $F_{SP} \sim F_{PP} \sim 0$, the expressions of ω_-^+ are determined (S12) with Det $\mathbf{A} = 0$.

$$\omega_-^+ = \bar{\omega} \pm \frac{1}{2}\text{Re}\left[\sqrt{4g^2 + \left[\omega_{SP} - \omega_{PP} + i\left(\frac{\Gamma_{SP}}{2} - \frac{\Gamma_{PP}}{2}\right)\right]^2}\right] \quad \text{(S12)}$$

VII. Dielectric Functions (h-BN, SiO_2 and Au)

The dispersion curves shown in the main text depend on the electrical permittivities of the materials that have dependence on ω. For h-BN[10,11], $\varepsilon_{xx}^{hBN}(=\varepsilon_{yy}^{hBN})$ and ε_{zz}^{hBN} components are given by eq. S13, with $\rho = xx$ and zz. $\varepsilon_{\rho,\infty}^{hBN}$ is the asymptotic permittivity value for high frequencies and Γ_{ρ}^{hBN} is the dielectric loss. For ε_{zz}^{hBN} in the hBN lower RS band that is resonant with out-of-plane (z direction) phonons, $\omega_{TO}^{zz} = 750\ cm^{-1}$, $\omega_{LO}^{zz} = 820\ cm^{-1}$, $\varepsilon_{\infty}^{zz} = 2.95$ and $\Gamma_{zz} = 3\ cm^{-1}$. For the hBN upper RS band resonant with in-plane (x direction), $\omega_{TO}^{xx} = 1365\ cm^{-1}$, $\omega_{LO}^{xx} = 1610\ cm^{-1}$, $\varepsilon_{\infty}^{xx} = 4.9$ and $\Gamma_{xx} = 5\ cm^{-11}$.

$$\varepsilon_{\rho}^{hBN} = \varepsilon_{\infty}^{\rho}\left(1 + \frac{(\omega_{LO}^{\rho})^2 - (\omega_{TO}^{\rho})^2}{(\omega_{TO}^{\rho})^2 - \omega^2 - i\omega\Gamma_{\rho}}\right) \qquad \text{(S13)}$$

In the case of SiO_2, the permittivity ε_{SiO_2} is a summation over multiple resonances featuring multiple peaks near ω_1 = 1090 cm^{-1}, ω_1 = 805 cm^{-1} and ω_3 = 457 cm^{-1}. $\varepsilon_{\infty} = 2.2$ is the high frequency permittivity. The equation S14 describes the model used, where S_1= 0.452, S_2 = 0.093 and S_3=1.022. Γ_1= 15, Γ_2= 10 and Γ_3= 10 are the crystal dielectric loss of each resonance

$$\varepsilon_{SiO_2} = \varepsilon_{\infty} + \frac{S_1{\omega_1}^2}{{\omega_1}^2 - \omega^2 - i\omega\Gamma_1} + \frac{S_2{\omega_2}^2}{{\omega_2}^2 - \omega^2 - i\omega\Gamma_2} + + \frac{S_3{\omega_3}^2}{{\omega_3}^2 - \omega^2 - i\omega\Gamma_3} \qquad \text{(S14)}$$

For the metallic media, ε_{Au} follows the Drude model[12,13], where ω_p=8.45 eV/$\hbar$ and $\Gamma_{\mathrm{Au}} = {}^{1}/_{\tau_D}$, with τ_D = 14 ps, are the plasmonic frequency and plasmonic damping, respectively.

$$\varepsilon_{Au} = 1 - \frac{\omega_p^2}{\omega^2 + i\omega\Gamma_{\mathrm{Au}}} \qquad \text{(S15)}$$

VIII. References

1. Casses, L. N. *et al.* Full Quantitative Near-Field Characterization of Strongly Coupled Exciton–Plasmon Polaritons in Thin-Layered WSe $_2$ on a Monocrystalline Gold Platelet. *ACS Photonics* **11**, 3593–3601 (2024).

2. Hu, F. *et al.* Imaging exciton–polariton transport in MoSe2 waveguides. *Nat Photonics* **11**, 356–360 (2017).

3. Zhou, Y. *et al.* Thermal and electrostatic tuning of surface phonon-polaritons in LaAlO3/SrTiO3 heterostructures. *Nat Commun* **14**, 7686 (2023).

4. Walla, F. *et al.* Anisotropic excitation of surface plasmon polaritons on a metal film by a scattering-type scanning near-field microscope with a non-rotationally-symmetric probe tip. *Nanophotonics* **7**, 269–276 (2018).

5. Mancini, A. *et al.* Near-Field Retrieval of the Surface Phonon Polariton Dispersion in Free-Standing Silicon Carbide Thin Films. *ACS Photonics* **9**, 3696–3704 (2022).

6. Maier, S. A. *Plasmonics: Fundamentals and Applications*. (Springer US, New York, NY, 2007). doi:10.1007/0-387-37825-1.

7. Bylinkin, A. *et al.* Real-space observation of vibrational strong coupling between propagating phonon polaritons and organic molecules. *Nat Photonics* 3–9 (2020) doi:10.1038/s41566-020-00725-3.

8. Autore, M. *et al.* Boron nitride nanoresonators for phonon-enhanced molecular vibrational spectroscopy at the strong coupling limit. *Light Sci Appl* **7**, 17172 (2018).

9. Pons-Valencia, P. *et al.* Launching of hyperbolic phonon-polaritons in h-BN slabs by resonant metal plasmonic antennas. *Nat Commun* **10**, 1–8 (2019).

10. Li, P. *et al.* Optical nanoimaging of hyperbolic surface polaritons at the edges of van der Waals materials. *Nano Lett* **17**, 228–235 (2017).

11. Dai, S. *et al.* Hyperbolic Phonon Polaritons in Suspended Hexagonal Boron Nitride. *Nano Lett* **19**, 1009–1014 (2019).

12. Steinberger, B. *et al.* Dielectric stripes on gold as surface plasmon waveguides. *Appl Phys Lett* **88**, 1–4 (2006).

13. Feres, F. H., Mayer, R. A., Barcelos, I. D., Freitas, R. O. & Maia, F. C. B. Acceleration of Subwavelength Polaritons by Engineering Dielectric-Metallic Substrates. *ACS Photonics* **7**, 1396–1402 (2020).